Int. J. Solids Structures Vol. 29, No. 9, pp. 1117–1142, 1992
Printed in Great Britain.

0020–7683/92 $5.00 + .00

BIFURCATION AND LOCALIZATION INSTABILITIES IN CYLINDRICAL SHELLS UNDER BENDING—I. EXPERIMENTS

S. KYRIAKIDES and G. T. JU
Engineering Mechanics Research Laboratory, Department of Aerospace Engineering and Engineering Mechanics, The University of Texas at Austin, Austin, TX 78712, U.S.A.

(*Received* 10 *January* 1991; *in revised form* 4 *August* 1991)

Abstract—This two-part series of papers is concerned with the response and various instabilities which govern the behavior of circular cylindrical shells under pure bending. Part I describes the experimental part of the study and Part II presents the numerical simulation of the various phenomena observed experimentally. Experiments were conducted on long aluminum 6061-T6 shells with 11 different diameter-to-thickness ratios ranging from 60.5 to 19.5. For such geometries, the structural response and inherent instabilities are strongly influenced by the plastic characteristics of the material.

Thinner shells were found to develop short wavelength periodic ripples on the compressed side of the shell. The shells buckled locally and collapsed soon after the appearance of the ripples. Thicker shells were found to exhibit a limit load instability as a direct consequence of the ovalization of the shell cross-section caused by bending. Following the limit load, the ovalization was found to localize, leading to the eventual collapse of the shells. For shells with intermediate D/t values, short wavelength ripples developed at the same time as localization of ovalization was recorded. The shells buckled locally and catastrophically following the development of a limit load.

NOMENCLATURE

D	shell outside diameter
D_{max}, D_{min}	maximum and minimum shell diameter
D_0	shell mean diameter
E	Young's modulus
L	shell half length
M	moment
M_0	$\sigma_0 D_0^2 t$
n	Ramberg–Osgood hardening parameter
S	anisotropy parameter
t	shell wall thickness
t_{max}, t_{min}	maximum and minimum wall thickness
Δ_0	initial ovality $\left(=\dfrac{D_{max}-D_{min}}{D_{max}+D_{min}}\right)$
ε_b, ε_L, ε_c	maximum Saint-Venant bending strain at bifurcation, limit load and collapse
κ	curvature
κ_1	t/D_0^2
κ_b, κ_L, κ_c	bifurcation, limit load and collapse curvature
λ	axial ripple half-wave length
λ_D	half-wave length of predicted ripples (J_2 deformation theory)
σ_y	Ramberg–Osgood yield parameter
σ_0	yield stress
Ξ_0	thickness variation parameter $\left(=\dfrac{t_{max}-t_{min}}{t_{max}+t_{min}}\right)$.

INTRODUCTION

This study is concerned with the problem of bending of long, circular cylindrical shells. Of particular interest is the response of such shells, bent into the plastic range of the material, and the various instabilities which limit the extent to which the shells can be loaded or deformed.

It is well known that bending of relatively thin-walled circular tubes induces ovalization to the tube cross-section (Brazier effect, 1927). The growth of ovalization causes a pro-

gressive reduction in the bending rigidity of the shell. Eventually, a maximum value of moment is reached. Further bending occurs at a dropping moment. For linearly elastic shells, when the maximum moment is reached the shell has undergone an ovalization which reduces the diameter of the cross-section in the plane of bending by approximately 2 9ths. In practice, for thin shells, this limit load instability is often preceded by shell bifurcation-type instabilities characterized by circumferential and axial waves [see Stephens *et al.* (1975), Fabian (1977) and Axelrad (1980)].

In the case of thicker shells ($D/t < 100$, say), the response, as well as the instabilities, are strongly influenced by interaction between the induced ovalization and the plastic characteristics of the material. Ades (1957) calculated the non-linear moment–curvature response of long elastic–plastic tubes undergoing uniform ovalization. He assumed the cross-section to deform into an ellipse and used the J_2 deformation theory of plasticity to model the non-linear material response. Gellin (1980) developed a more accurate solution to the problem using improved kinematics and the J_2 deformation theory of plasticity. Gellin's formulation and solution procedure were further refined by Shaw and Kyriakides (1985) by adopting a more complete set of extensional kinematics and incremental plasticity models [see also Fabian (1981) and Bushnell (1981)].

These solutions demonstrated that, although the ovalization imposed on the shell cross-section is relatively small for shells bent into the plastic range, it still leads to the development of a limit moment in the response. This is demonstrated in Fig. 1, where three moment–curvature responses for an aluminum shell with a diameter-to-thickness ratio (D/t) of 35.7 are compared. One of the responses shown was obtained by simple integration of the stresses through the cross-section (Saint-Venant bending); as a result the moment is monotonically increasing. The second response was calculated by a Brazier-type analysis, which includes the effect of the ovalized cross-section. It has a somewhat lower moment but, more importantly, the ovalization results in the development of a limit moment.

Experiments involving pure bending of inelastic shells have been carried out by Moore and Clark (1952), Jirsa *et al.* (1972), Sherman (1976), Tuggu and Schroeder (1979), Reddy (1979), Kyriakides and Shaw (1987) and others. Johns *et al.* (1975), Corona and Kyriakides (1988) and Ju and Kyriakides (1991) carried out experiments involving combined bending and external pressure.

The experiments demonstrated that, in addition to the limit load instabilities, shell bending is limited by various shell buckling modes. In addition, evidence of distinct localization of deformation was observed in many shells [see Fig. 6 in Corona and Kyriakides (1988)]. Figure 1 includes the moment–curvature response obtained from an experiment on an aluminum 6061-T6 shell with $D/t = 35.7$. The shell was found to ovalize uniformly for most of the bending history. At the curvature indicated by (↓) short wavelength ripples were observed on the compressed side of the shell. Soon after the ripples appeared, the

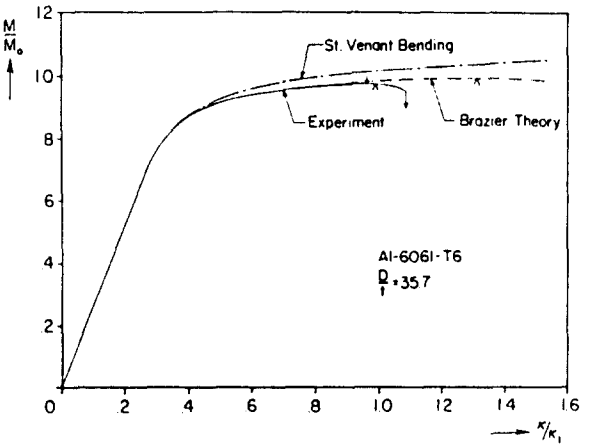

Fig. 1. Moment–curvature responses of aluminum tube ("∧" ≡ limit moment; "↓" ≡ short wavelength rippling).

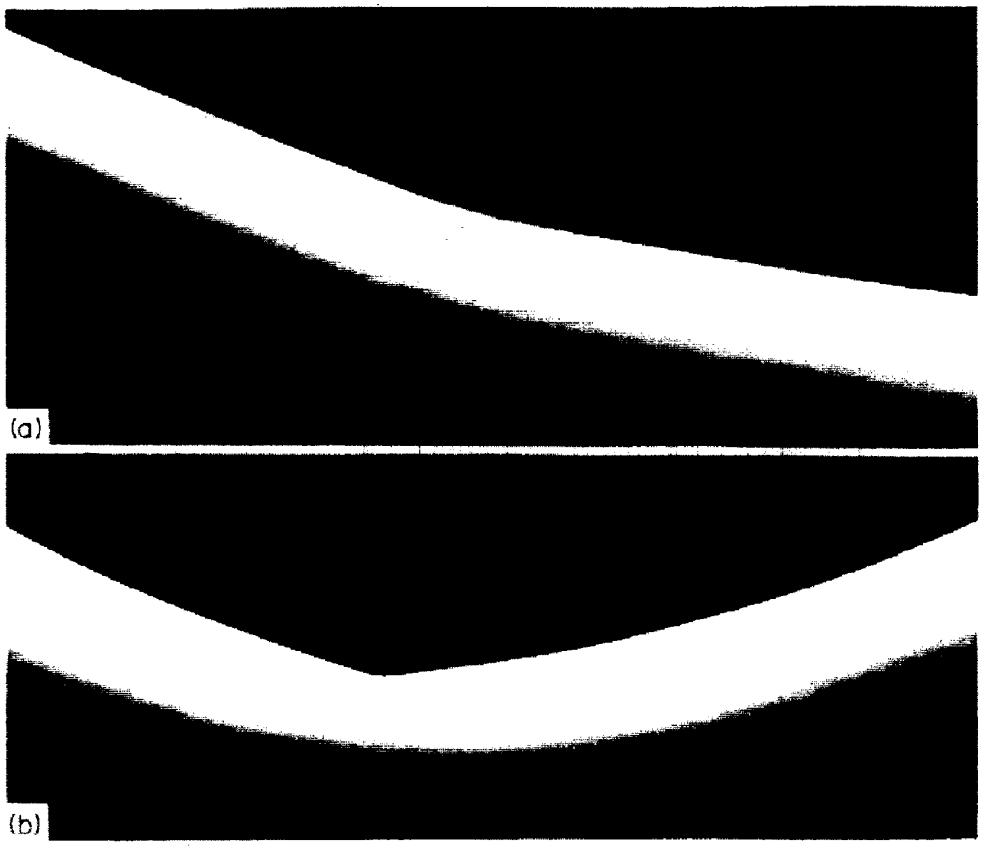

Fig. 2. (a) Local buckle caused by bending in shell with $D/t = 35.7$. (b) Localization of ovalization in shell with $D/t = 19.5$.

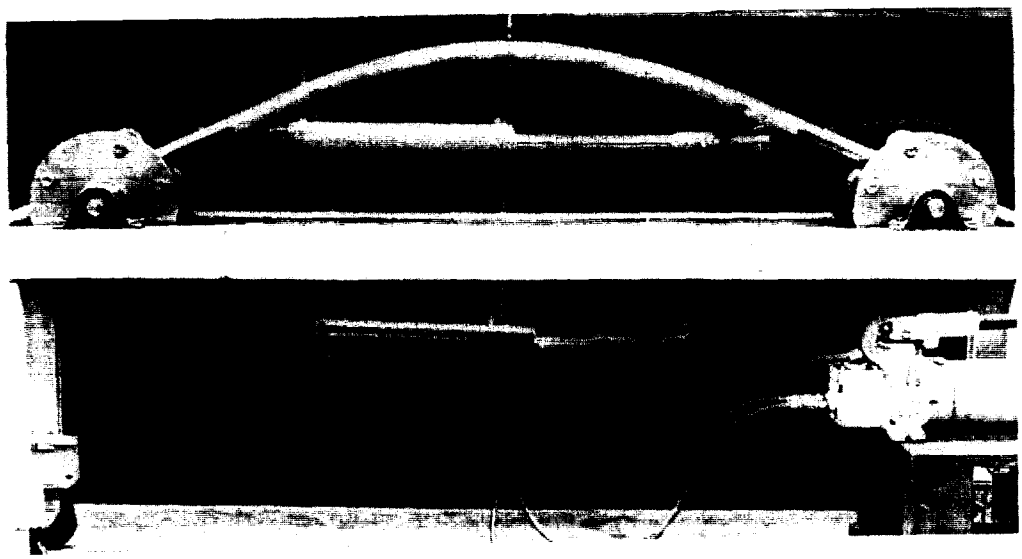

(a)

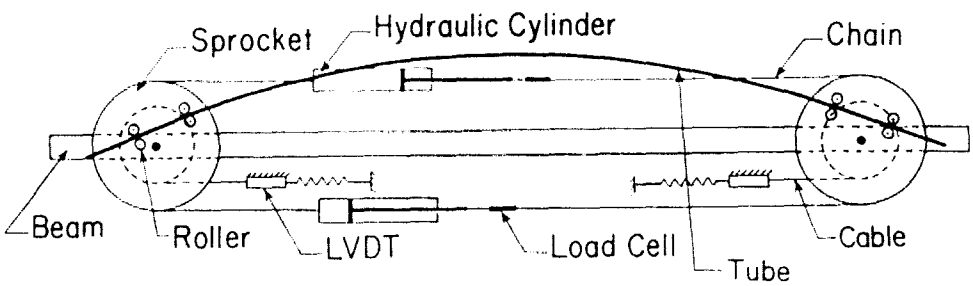

(b)

Fig. 4. (a) Pure bending test facility. (b) Schematic of test facility.

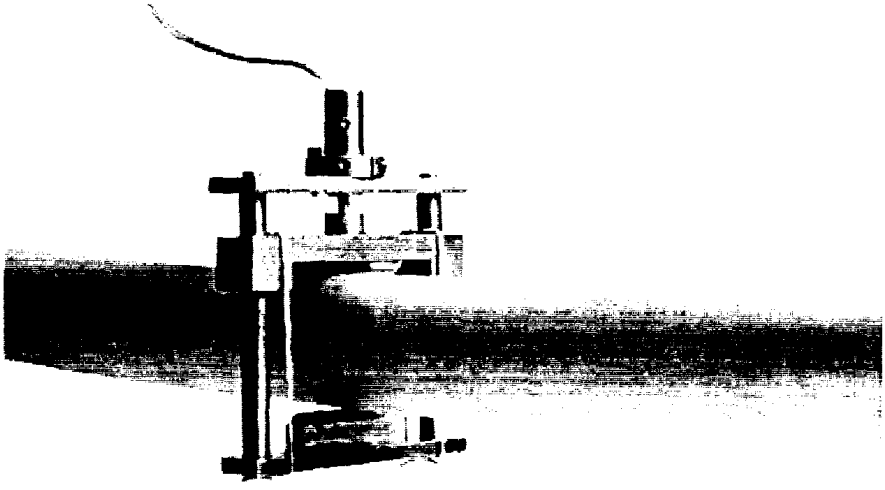

Fig. 6. Stationary ovalization transducer.

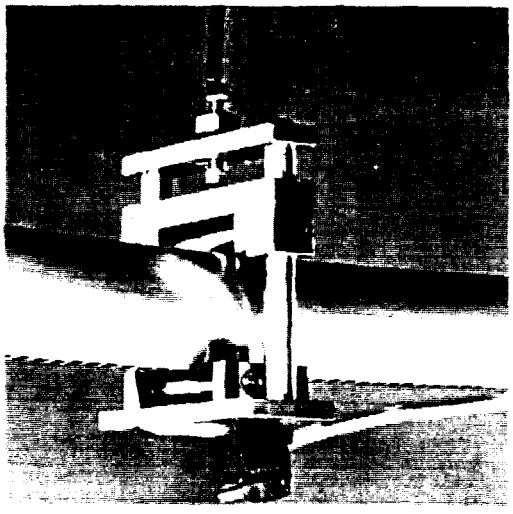

(a)

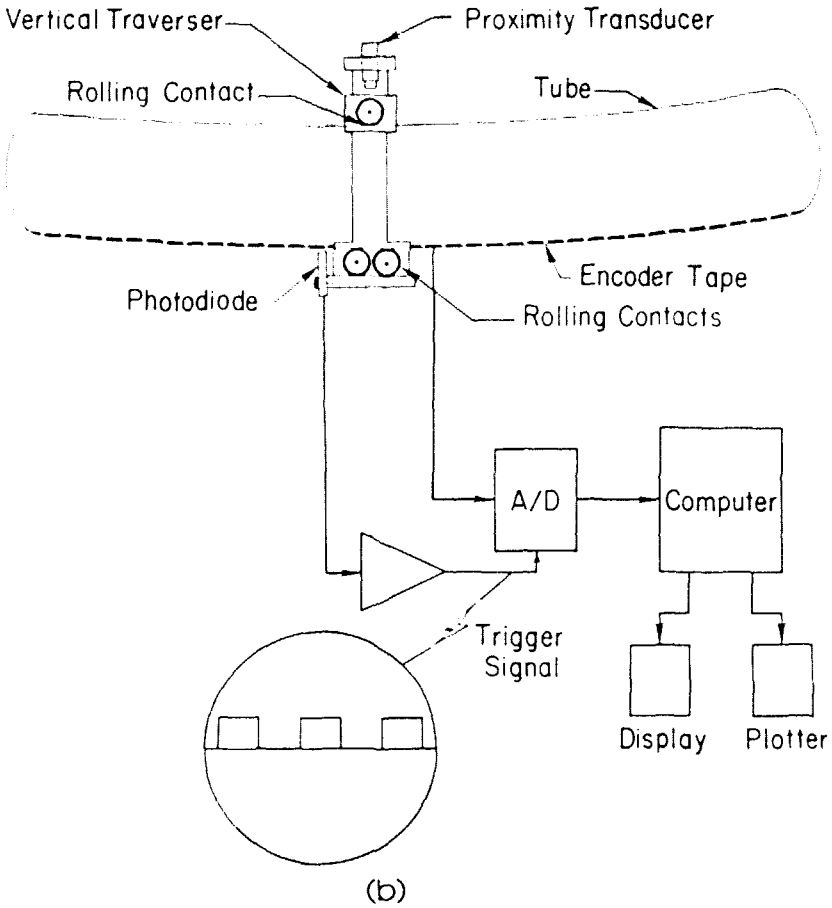

(b)

Fig. 7. (a) Transducer for scanning ovalization along shell length. (b) Transducer schematic and A/D converter triggering circuit.

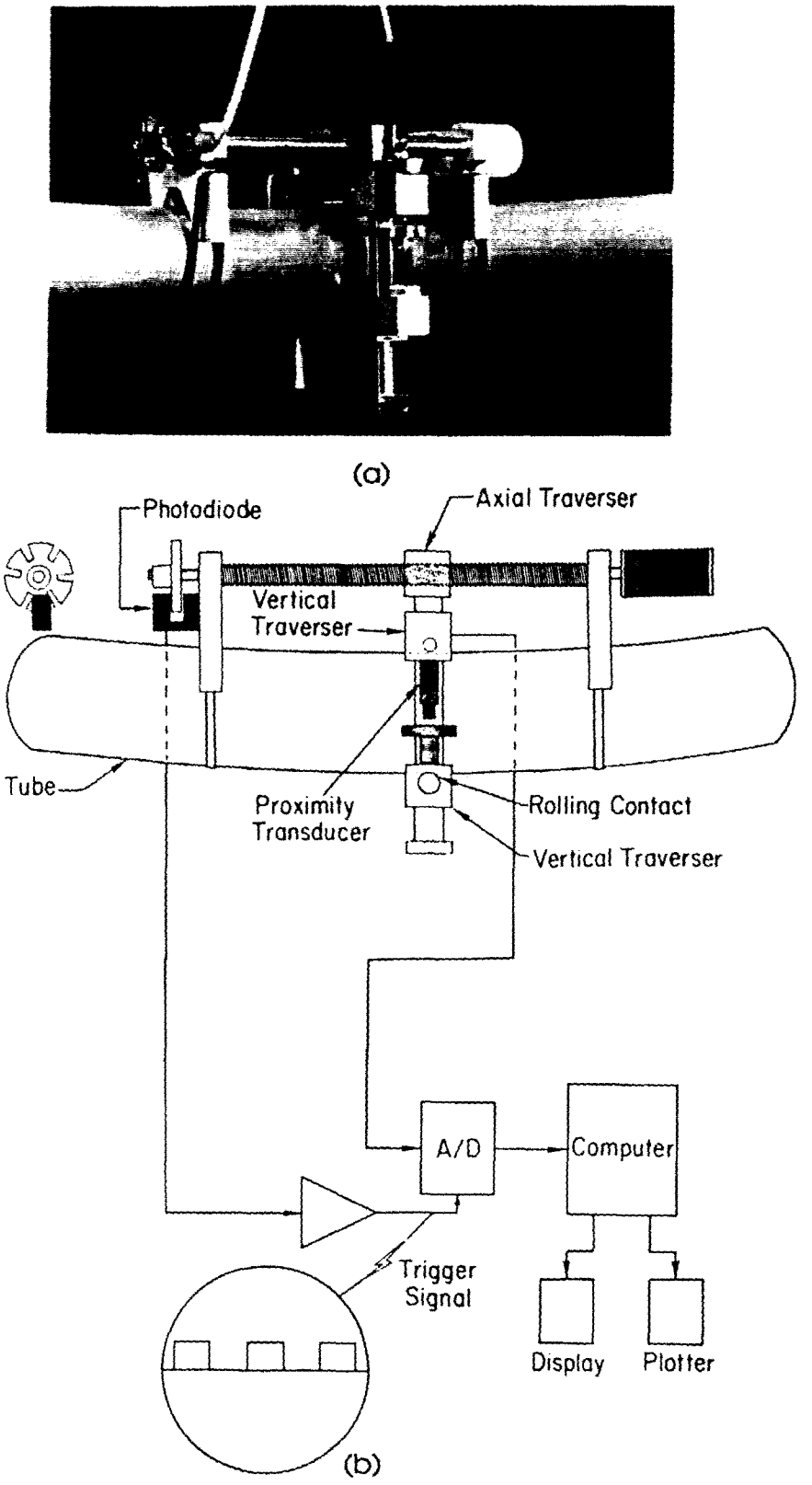

Fig. 8. (a) Ovalization transducer with high axial resolution. (b) Transducer schematic and A/D converter triggering circuit.

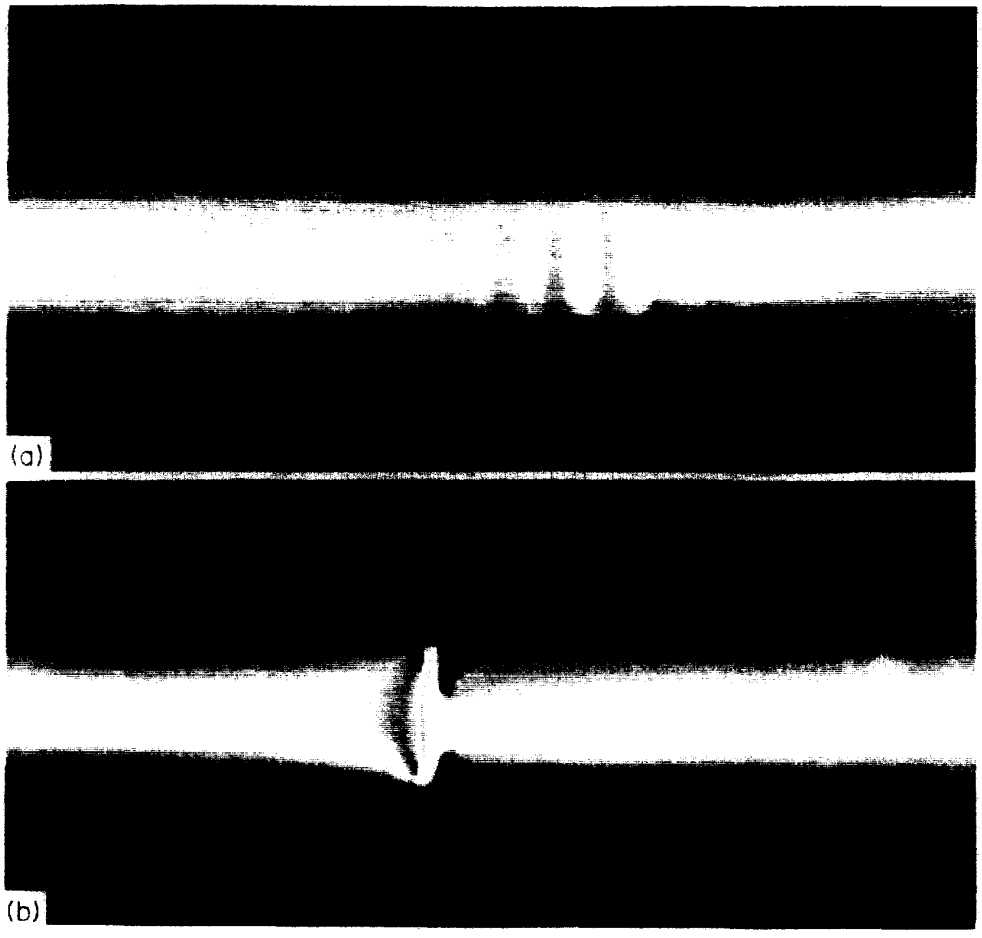

Fig. 9. (a) Axial ripple developed on compression side of shell in pure bending ($D/t = 32.2$). (b) Local buckle which occurs shortly after the ripples developed ($D/t = 44$).

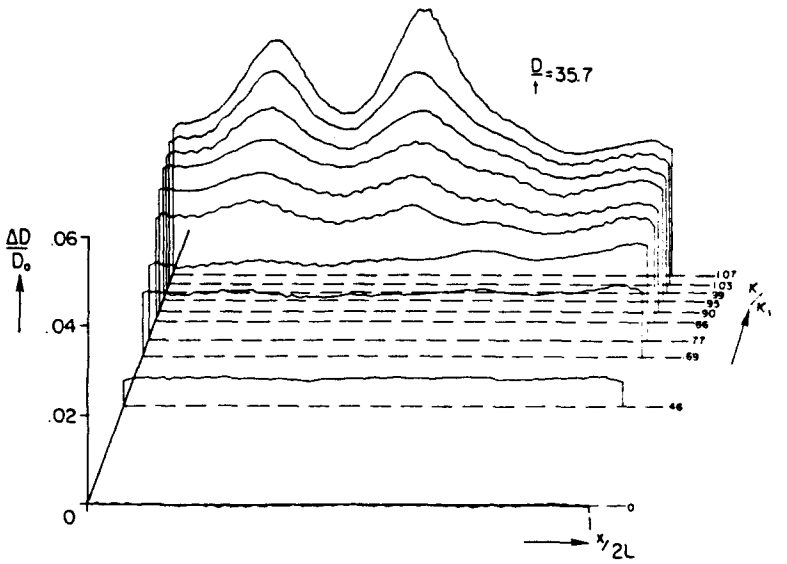

Fig. 3. Ovalization along shell length for different values of curvature [Aluminum-6061-T6; $D/t = 35.7$. Experiment by S. Kyriakides and R. Juarez (1982) unpublished].

ovalization started to localize in a region approximately eight shell diameters long, a limit load developed on the response (identified by "∧") and the shell buckled locally at a dropping moment. A buckled test specimen is shown in Fig. 2a. As the limit load was approached, it was observed that long wavelength initial imperfections in the shell tended to be amplified. This resulted in some non-uniform growth of ovalization. An example of this behavior is shown in Fig. 3 where axial scans of the change in diameter in the shell ($\Delta D/D_0$), in the plane of bending, taken at different values of curvature are shown. The shell cross-section ovalized in a reasonably uniform manner up to a curvature of $\kappa/\kappa_1 = 0.80$. At higher curvatures, long wavelength axial waves are seen to develop. The shell failed catastrophically by local buckling in one of the troughs of ovalization.

Clearly the behavior described above is different and more complicated than what has been modelled in the references mentioned above. The objective of this study was to identify and understand the role of the major instabilities which affect the response of long elastic plastic shells under pure bending. This was done through a combination of experiment and analysis. A systematic set of experiments was conducted using aluminum shells with a broad range of diameter-to-thickness ratios. The experimental facilities used, procedures followed, the results from the experiments and a discussion of the observations are presented in Part I. The major phenomena observed in the experiments are simulated numerically in Part II. The numerical predictions are used to explore and explain the behavior of the structures tested.

EXPERIMENTS

(1) *Test facilities*

The bending experiments were conducted in a test facility consisting of a pure bending device, shown in Fig. 4, various transducers for recording geometric changes in the shell and a computer-based data acquisition system. The bending device was designed as a four-point bending machine capable of applying bending and reverse bending [see Kyriakides and Shaw (1987)]. It consists of two double strand sprockets [pitch diameter 9.56 in (243 mm)] mounted with pillow blocks on two parallel beams as shown in Fig. 5. The beams are 70 in (1.78 m) long and the distance between the sprockets can be varied. In the experiments described here the sprockets were located 49.5 in (1.26 m) apart. Heavy chains run around the sprockets and are connected to hydraulic cylinders and load cells forming a closed loop. For monotonic bending, the bending curvature capacity of the machine can

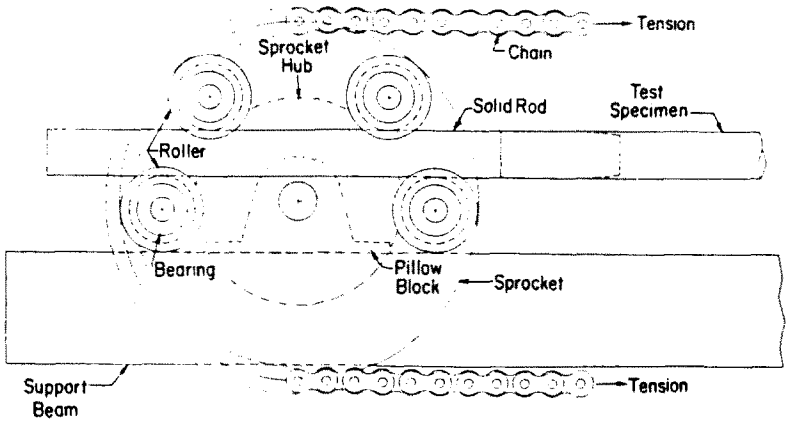

Fig. 5. Detail of load transfer mechanism.

be doubled by removing one of the cylinders and extending the second one to its full stroke of 10 in (0.25 m).

Each test specimen is fitted with close-fitting solid extension rods, as shown in Fig. 5. The rods extend more than three diameters into the free ends of the shell and are carefully chamfered at the ends to reduce the effect of the discontinuity. The test specimen assembly engages the sprockets through four rollers, as shown in the figure.

Bending is achieved by contracting one of the hydraulic cylinders, causing rotation of the sprockets. During bending, the rolling contact between the end rods and the test facility allows free axial movement of the test specimen. While the deformation of the test specimen is uniform along the length, the bending curvature is directly proportional to the rotation of the two sprockets. The rotation of each sprocket is monitored by a linear voltage differential transformer (LVDT) as follows: A flexible, inextensional, thin cable runs over the circular hub of the sprocket. The cable is spring loaded and is connected to the core of the LVDT. Thus, rotation causes linear movement of the core and a proportional signal from the LVDT.

The majority of the test specimens tested had an effective length of 30 in (0.76 m). With the test facility configuration used such specimens could be bent to a curvature of 0.070 in^{-1} (2.75 m^{-1}). Larger curvatures can be achieved by reducing the length of the shell.

The bending moment in the test specimen is directly proportional to the tension in the chain. This is monitored by calibrated load cells. The capacity of the bending device is 15,000 lb/in (1,700 N/m). The device was designed to be stiff relative to the test specimens. For the experiments reported here, the energy stored in the device was less than 4.5% of the energy stored in the strongest of the test specimens (approximately half of this is stored in the hydraulic system). A stiff machine is essential for testing structures beyond limit loads.

The ovalization of the cross-section of the tube is known to play an important role in the stability of the structure. Thus, several transducers for monitoring small changes in the geometry of the shell during bending were developed. Figure 6 shows a lightweight transducer which is mounted on the shell and used to monitor changes in the diameter in the plane of bending. It consists of a rigid frame which supports a sliding block. The instrument is lightly spring loaded, as shown in the figure, and contacts the shell through knife edges. The relative displacement between the two knife edges is monitored by a miniature LVDT. In some experiments, two such transducers, placed approximately ten shell diameters apart, were used in order to establish the onset of localized deformation in the shell.

A computer-based data acquisition system was used to monitor the variables measured during the experiment. It consists of several signal conditioning units, an analog-to-digital (A/D) converter, a desktop computer and peripherals such as digital plotters and a monitor. The system enables real time display of some of the variables and provides storage of the data for later analysis.

During a typical monotonic bending experiment on a shell, the variables monitored were the moment (M), the curvature (κ) and the ovalization at one or two discrete points along the length of the shell (ΔD_i). The data acquisition system stores a set of $\{M, \kappa, \Delta D_i\}_j$ whenever any one of the variables changes by a prescribed small value. The number of sets of data collected from each experiment varied from approximately 125 for the thinner shells to 450 for the thicker shells. The uncertainties in the recorded data were as follows: moment $\sim 0.8\%$; curvature $\sim 0.6\%$; ovalization $\sim 0.1\%$.

In at least one experiment for each shell D/t considered, a second transducer, shown in Fig. 7, was used to periodically scan the ovalization along the length of the shell. In this case, contact with the shell is made through rollers. The transducer is moved along the length of the shell manually. Its axial position is established by an encoder system which works as follows: a thin flexible tape, with regularly spaced black–white markings, is bonded on the tension side of the shell as shown in the figure. An emitter/receiver photodiode, mounted on the transducer, produces an electrical pulse whenever it encounters a white marking. The pulse, suitably processed, triggers the A D converter and the value of ovalization is recorded in the computer. In the majority of the experiments presented here, the encoder had a resolution of five readings per inch.

In the case of thinner shells, short wavelength *ripples* develop on the compression side of the bent shell. For the aluminum shells used in the experiments, with typical diameters between 1.0 and 1.5 in (25–38 mm), the amplitude of these ripples was of the order of 0.001–0.005 in (0.025–0.125 mm). Thus, a more sensitive instrument with higher axial resolution, shown in Fig. 8, was developed for measuring the geometry of these ripples. It consists of an axial guide, with a fine lead screw, which supports a vertical traversing system. This is lightly spring loaded and is in contact with the top and bottom of the shell through small diameter rollers. The guide is 4 in (102 mm) long and is mounted on the bent shell as shown in the figure. The vertical frame is moved axially by turning the lead screw. The two traversing beams are free to move vertically to accommodate changes in the geometry of the shell. Changes in the distance they are apart are monitored by a proximity, non-contact, displacement transducer with a sensitivity of 125 mV 10^{-3} in (4.92 V mm $^{-1}$). The axial position of the transducer is monitored by an encoder system which consists of an emitter/receiver photodiode and a circular disc with six equally-spaced narrow slits. The photodiode produces a pulse whenever the light beam is obstructed. The signal from the encoder is used to trigger the A/D converter and the computer stores the output of the proximity transducer. The axial resolution of the system provided for 192 readings per inch.

(2) *Experimental procedure*

The experiments were carried out on commercially available aluminum 6061-T6 drawn tubes. The test specimens had nominal diameters ranging from 1.0 in (25.4 mm) to 1.5 in (38.1 mm). Tubes with eleven different diameter-to-thickness ratios, ranging from 60.5 to 19.5, were tested. The (effective) lengths of the test specimens were 30 in (0.76 m); thus, their length-to-diameter ratios ranged between 18 and 30. Average values of the diameters and wall thicknesses of the test specimens, as well as their lengths, are listed in Table 1. In each case, enough measurements were made to also establish the maximum value of initial ovalization along the length of the tube. The maximum value of ovalization measured, Δ_0, is defined as follows:

$$\Delta_0 = \frac{D_{max} - D_{min}}{D_{max} + D_{min}}. \tag{1}$$

The values of Δ_0 measured in each shell are listed in Table 1. Wall thickness variations measured at the two ends of the test specimens are also given by their extreme value Ξ_0 defined as follows:

$$\Xi_0 = \frac{t_{max} - t_{min}}{t_{max} + t_{min}}. \tag{2}$$

The material properties of each tube tested were measured from uniaxial tests on axial

Table 1. Geometric and material characteristics of shells tested

Exp. No.	D, in (mm)	D/t	Δ_0%	Ξ_0%	$2L/D$	E, ksi (GPa)	σ_0, ksi (MPa)	σ_y, ksi (MPa)	n	S
1	1.253 (31.82)	60.5	0.06	1.70	24.0	10.0×10^3 (68.95)	43.4 (299)	43.3 (298.6)	28	—
2	1.500 (38.10)	52.6	0.13	1.41	18.1	10.1×10^3 (69.64)	43.4 (299)	43.3 (298.6)	33	—
3	1.000 (25.40)	50.0	0.12	3.90	30.0	10.3×10^3 (70.67)	44.5 (307)	44.6 (307.5)	29	0.90
4	1.251 (31.78)	44.0	0.12	4.50	24.0	9.75×10^3 (67.20)	44.1 (304)	44.0 (303.4)	25	0.92
5	1.378 (35.00)	38.5	0.07	0.04	21.8	10.3×10^3 (71.02)	41.6 (287)	41.4 (285.4)	25	—
6	1.250 (31.75)	35.7	0.05	0.86	24.0	9.77×10^3 (67.36)	41.1 (283.4)	40.9 (282.0)	28	0.91
7	1.127 (28.63)	32.2	0.05	2.89	26.1	10.3×10^3 (71.16)	41.7 (288)	41.5 (286.1)	26	0.95
8	0.998 (25.34)	28.2	0.06	0.99	30.1	9.60×10^3 (66.20)	44.1 (304)	44.0 (303)	35	—
9	1.252 (31.80)	25.3	0.06	1.21	24.0	10.0×10^3 (69.16)	41.5 (286)	41.3 (284.8)	30	0.93
10	1.251 (31.78)	21.2	0.09	3.19	24.0	10.3×10^3 (71.16)	41.4 (285)	41.2 (284.1)	28	—
11	1.251 (31.78)	19.5	0.05	3.45	24.0	9.96×10^3 (68.67)	44.8 (309)	44.8 (308.9)	37	—

specimens cut from the same length of tube as the bending specimens. The stress–strain curves obtained were fitted with the Ramberg–Osgood fit given by

$$\varepsilon = \frac{\sigma}{E}\left[1 + \frac{3}{7}\left(\frac{\sigma}{\sigma_y}\right)^{n-1}\right]. \tag{3}$$

The fit parameters calculated from each test specimen are listed in Table 1. In addition, the 0.2% strain offset yield stress (σ_0) is listed for each case. In a number of the test specimens, an additional experiment was conducted through which the yield stress in the circumferential direction was established [as in Kyriakides and Yeh (1988)]. The variable S represents the ratio of the yield stress in the circumferential to that in the axial direction (the yield stress in the thickness direction was assumed to be the same as that in the axial direction).

A minimum of two experiments were conducted for each D/t considered. The first involved monotonic bending of the test specimen at a strain rate (maximum) of approximately 1% min^{-1}. Each specimen was loaded to failure.

In the second experiment, the bending was periodically interrupted. The flow to the hydraulic cylinder was shut and then an ovalization scan was conducted. Six to 12 such scans were taken during the bending history. During every interruption of the loading, the compressed side of the shell was visually inspected for the possible appearance of ripples. When such ripples were detected, the instrument, shown in Fig. 8, was installed on the test specimen and used to conduct a detailed examination of the area in which they appeared. Ripples usually appeared in pockets of two to four randomly distributed along the length. Figure 9a shows a picture of two such pockets of ripples for test specimen No. 7. The range of curvature during which the ripples were visible was rather limited. Soon after their appearance, the shell buckled catastrophically, developing one distinct local buckle. An example of such a buckle is shown in Fig. 9b. Following such a buckle, the bending capacity of the shell usually dropped by 80 or 90%.

RESULTS

The experimental results will be presented in non-dimensional form using the following normalizing parameters:

Table 2. Critical deformations of shells tested

Exp. No.	D/t	κ_b/κ_1 (ε_b%)	κ_L/κ_1 (ε_L%)	κ_c/κ_1 (ε_c%)	$\lambda/\sqrt{Dt}$
1	60.5			0.93 (0.79)	
2	52.6			1.00 (0.95)	
3	50.0	0.91 (0.97)		0.95 (1.01)	0.997
4	44.0	0.95 (1.13)		1.06 (1.26)	1.193
5	38.5	0.95 (1.26)		1.00 (1.32)	0.887
6	35.7	0.96 (1.42)	0.99 (1.49)	1.09 (1.61)	0.717
7	32.2	0.94 (1.58)	0.94 (1.58)	1.02 (1.72)	0.872
8	28.2	0.89 (1.69)	0.90 (1.72)	1.07 (2.04)	0.718
9	25.3		0.95 (2.03)	1.05 (2.25)	
10	21.2		0.98 (2.55)	1.17 (3.05)	
11	19.5		0.95 (2.79)	1.24 (3.54)	

$$M_0 = \sigma_0 D_0^2 t, \quad \kappa_1 = t/D_0^2. \tag{4}$$

The curvature at which ripples were first detected on the compressed side of the shell is identified by κ_b, in Table 2, and by the symbol (↓) in the figures. (Note that κ_b was usually obtained from the second bending experiment in which bending was interrupted while the shell was checked for ripples. Thus the search was discrete and as a result the values of κ_b recorded are in general somewhat larger than the actual values.) The curvature at which the maximum moment was achieved (limit moment) is identified by κ_L in Table 2 and by the symbol (∧) in the figures. The curvature at which catastrophic collapse occurred is identified as κ_c and by the symbol (↓). For completeness, the maximum Saint-Venant bending strains corresponding to each of these critical curvatures (ε_b, ε_L, ε_c) are also included in the table.

The analysis developed by Shaw and Kyriakides (1985) was used to calculate the moment–curvature and ovalization–curvature responses for each of the experiments conducted. In this analysis, the shell is treated as a long tube whose cross-section can ovalize but is otherwise uniform along the axis. The analysis is thus capable of predicting the limit load instability inherent in the problem. The predictions from this analysis are shown by a dashed line in each of the figures.

The moment–curvature and ovalization–curvature responses from the test specimen with the largest value of D/t tested ($D/t = 60.5$) are shown in Fig. 10. The shell buckled catastrophically at a curvature of $\kappa_c/\kappa_1 = 0.93$ which is equivalent to a maximum Saint-Venant bending strain of 0.79%. Buckling occurred at an increasing moment and took the form of one sharp, local buckle characterized by a number of diamond shapes on the compressed side of the shell, similar to the one shown in Fig. 9b (the diamond shapes are reminiscent of elastic buckling of shells). The ovalization measured along the length of the shell, at various values of curvature, are shown in Fig. 11. Apart from the boundaries, the ovalization is seen to remain essentially uniform along the length for all values of curvature shown. For this value of D/t, no axial ripples were detected for either of the shells tested.

The moment–curvature and ovalization–curvature responses predicted numerically are seen to be in very good agreement with the experimental ones. The curvature at which the limit load was predicted to occur is seen to be approximately 90% higher than the collapse curvature.

The behavior of the shell with $D/t = 52.6$ was very similar to that described above. The curvature and the bending strain at collapse are listed in Table 2. The major results

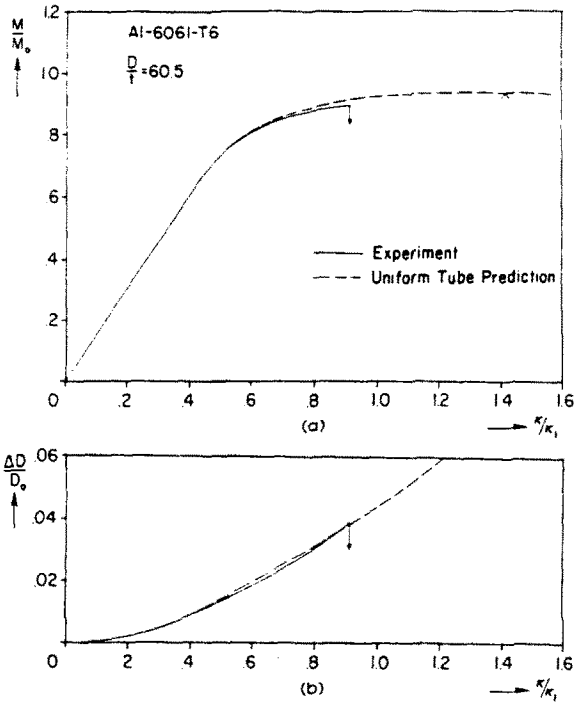

Fig. 10. Bending response of aluminum shell with $D/t = 60.5$: (a) Moment curvature. (b) Ovalization curvature.

from the shells with D/t values of 50 and 44 are shown in Figs 12–15. The major features of the responses are essentially the same. As the D/t decreases, the Saint-Venant bending strain and the curvature at collapse increase. In addition, the difference between the curvature corresponding to the predicted limit moment and that at collapse decreases.

Axial ovalization scans taken at different values of curvature are shown in Figs 13 and 15. The ovalization is seen to remain reasonably uniform throughout the bending history for both shells. In both cases, pockets of short wavelength ripples were detected on the compressed side of the shell just prior to catastrophic collapse. The location of one of the pockets is identified in the ovalization scans. A detailed scan of the ripple pocket is shown, in each case, in the inset. The average wavelength of the ripples measured, $\lambda/\sqrt{Dt}$, is given in Table 2.

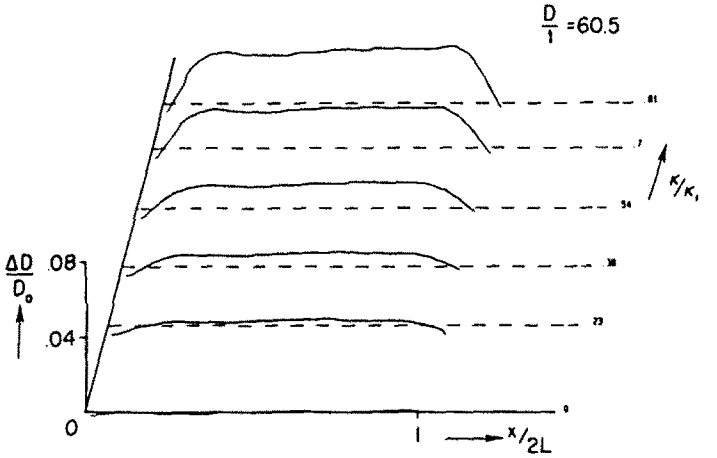

Fig. 11. Ovalization along shell length at different curvatures ($D/t = 60.5$).

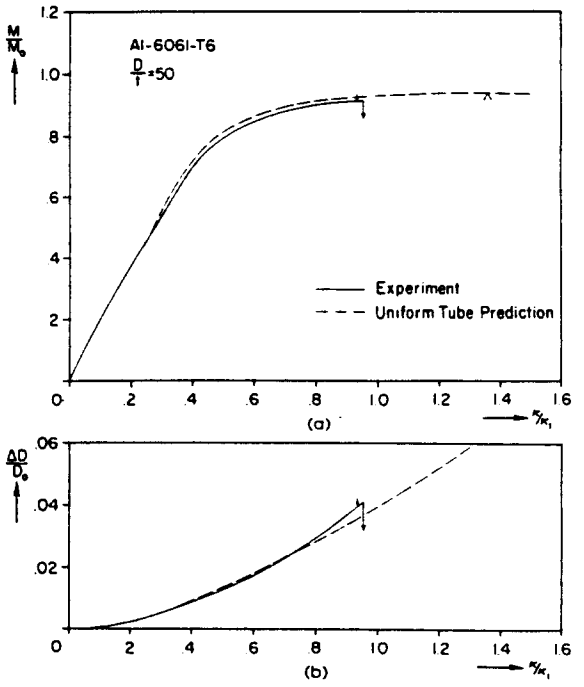

Fig. 12. Bending response of aluminum shell with $D/t = 50$: (a) Moment curvature. (b) Ovalization curvature.

Although the appearance of the ripples during the bending history was relatively short, in some cases it was possible to monitor their development by conducting local axial scans of the shell at small intervals of curvature. As the curvature increased the ripples grew in amplitude but remained fixed at their original position along the length of the shell. During the course of this study it was found that improperly designed load transfer mechanisms at

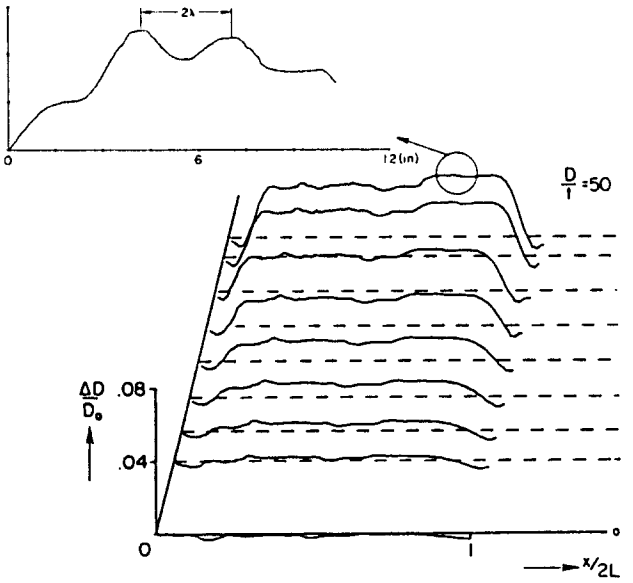

Fig. 13. Ovalization along shell length at different curvatures ($D/t = 50$; inset shows detail of short wavelength ripple).

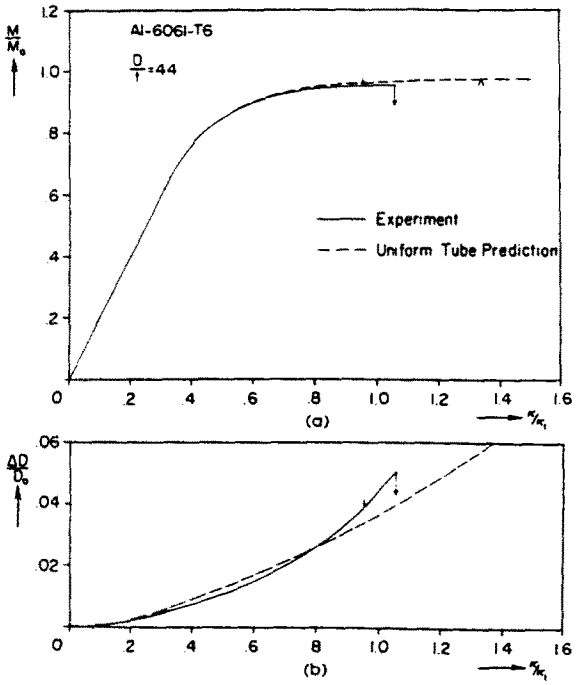

Fig. 14. Bending response of aluminum shell with $D/t = 44$: (a) Moment curvature. (b) Ovalization curvature.

the boundaries can result in premature buckling of the shell with the buckle developing at the ends.

Figures 16 and 17 show the results from a shell with $D/t = 35.7$. For this case, and for all other shells tested with lower D/t values, the axial scans of ovalization at different values of curvature produced evidence that, beyond a certain value of curvature, the ovalization started growing in a non-uniform fashion along the length. For example, in Fig. 17, it can be seen that the ovalization remained uniform up to a value of $\kappa/\kappa_1 = 0.81$. The beginning of some non-uniform growth is seen to occur at $\kappa/\kappa_1 = 0.93$. At the last value of curvature at which an axial scan was taken, $\kappa/\kappa_1 = 0.99$ (i.e. just prior to collapse), the ovalization is seen to grow significantly more in a region approximately eight diameters long. The

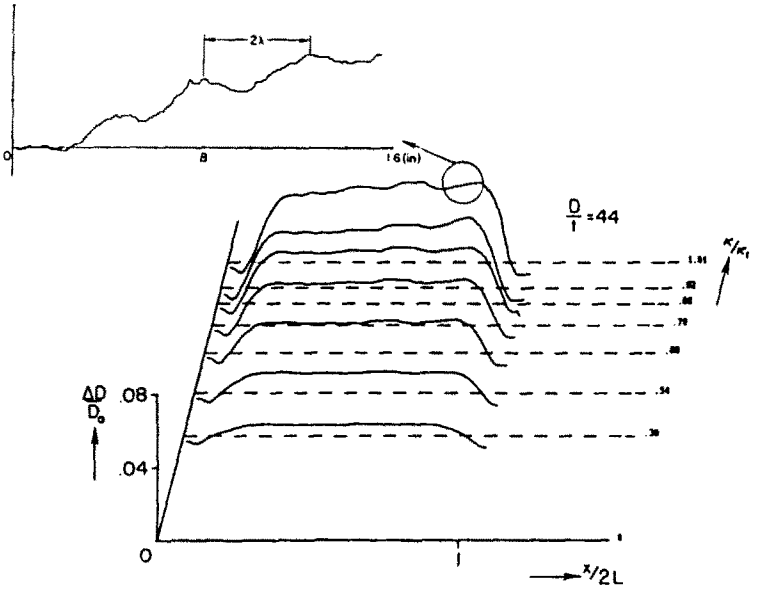

Fig. 15. Ovalization along shell length at different curvatures ($D/t = 44$; inset shows detail of short wavelength ripples).

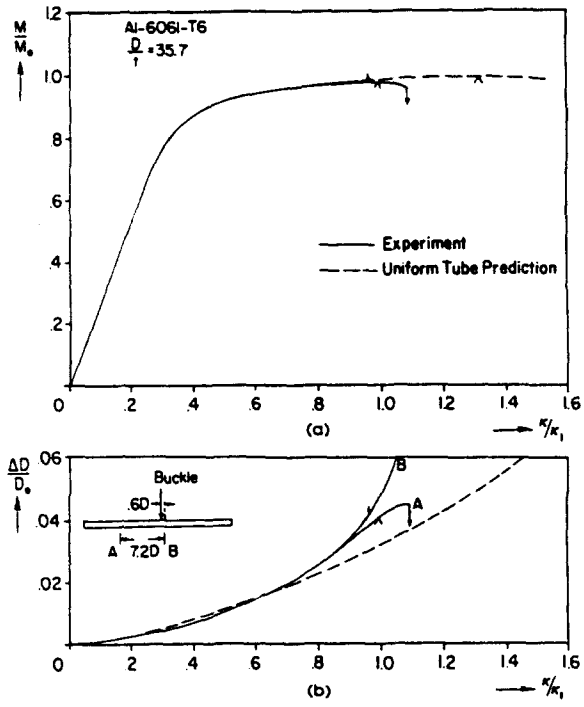

Fig. 16. Bending response of aluminum shell with $D/t = 35.7$: (a) Moment–curvature. (b) Ovalization–curvature.

maximum ovalization recorded is approximately twice the average value over the remainder of the shell. At a curvature of $\kappa_b/\kappa_1 = 0.96$, a pocket of short wavelength ripples became visible in the trough of the overly ovalized region. A detailed axial scan of this region is shown in the inset in Fig. 17. Further bending resulted in catastrophic buckling. The buckle was triggered by the ripples and had the form of one sharp, local kink, similar to the one shown in Fig. 2a.

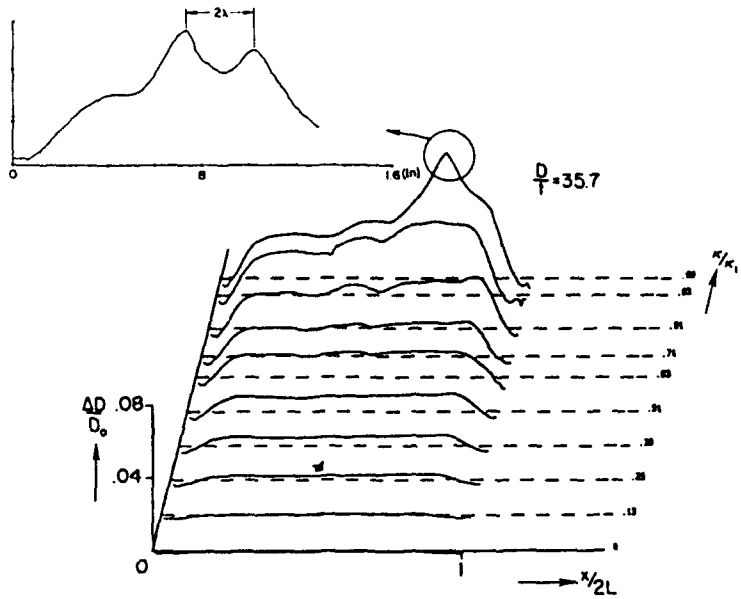

Fig. 17. Ovalization along shell length at different curvatures ($D/t = 35.7$; inset shows detail of short wavelength ripples).

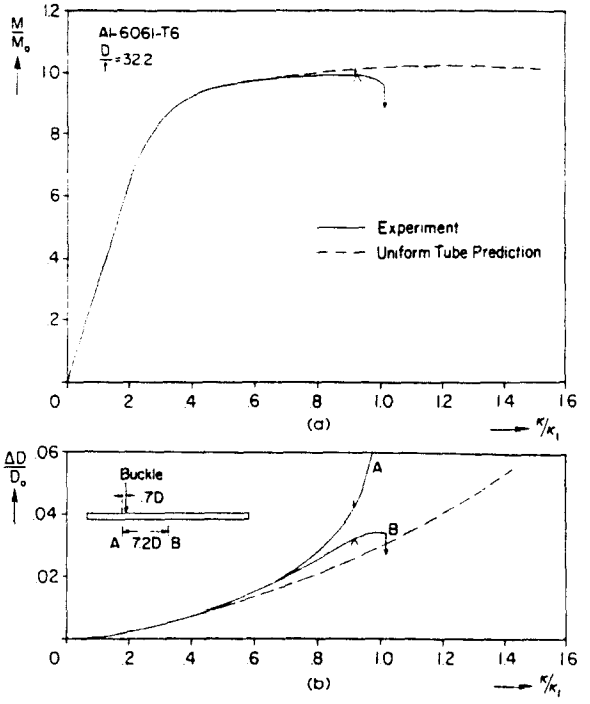

Fig. 18. Bending response of aluminum shell with $D/t = 32.2$: (a) Moment–curvature. (b) Ovalization curvature.

The moment curvature and ovalization curvature responses recorded for this shell are shown in Fig. 16 (different test specimen from that in Fig. 17). The moment-curvature response developed a limit moment at a curvature of $\kappa_L/\kappa_1 = 0.99$. The shell collapsed catastrophically at $\kappa_c/\kappa_1 = 1.09$. Due to the evidence of some localized deformation, two ovalization transducers, placed 7.2 shell diameters apart, were used in this experiment. Their axial positions, relative to the position of the final buckle, are shown in the inset in Fig. 16b. The measured ovalizations at the two points are seen to maintain the same value up to a curvature of approximately $\kappa/\kappa_1 = 0.9$. At higher values of curvature, the ovalization is seen to grow faster at point B than at point A. The proximity of point B to the position of the buckle, and the results from the experiment in Fig. 17, explain this behavior.

We observe that the limit load predicted by assuming the shell to remain uniform along its length is significantly higher than the actual limit load recorded in the experiment. We thus conclude that the causes of the two instabilities are probably different. We point out once more, that the cause of failure was again short wavelength buckling. Quite clearly, some interaction between the observed localization in ovalization and the short wavelength buckling mode does take place. It would be of interest to understand this interaction and its effect on the final curvature at collapse.

Figure 18 shows the structural response from a shell with $D/t = 32.2$. The main characteristics of the results are similar to those of the shell with $D/t = 35.7$. Because of the thicker wall, the difference between the measured and calculated curvatures at the corresponding limit moments is smaller. Short wavelength ripples were again observed prior to the limit load. Figure 19 shows four local axial scans of the diameter of the shell in the plane of bending taken in the curvature range of $\kappa/\kappa_1 = 0.934$ and $\kappa/\kappa_1 = 0.991$. The results illustrate the growth of a pocket of two ripples. The amplitude of the ripples is seen to grow as the curvature was increased; but their axial position remained fixed.

In the neighborhood of the limit load the shell again developed some localized ovalization (see Fig. 18b). The cause of the observed localization will be explored in the following paper. At this stage, it suffices to say that, for shells with intermediate values of D/t (i.e. approximately $26 < D/t < 40$), long wavelength imperfections tend to be amplified, to some degree, as the collapse curvature is approached. The result is localized growth of ovalization,

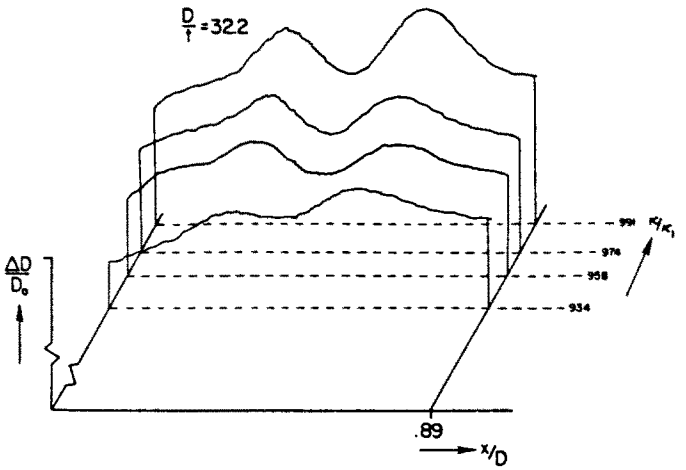

Fig. 19. Local scans of ovalization at different curvatures showing development of axial ripple ($D/t = 32.2$).

as shown in Figs 3 and 17. Similarly, areas with some stress concentration, such as might be caused by overly constraining boundary conditions, can also cause some non-uniform growth of ovalization.

A set of results obtained from a shell with $D/t = 25.3$ is shown in Figs 20 and 21. The measured moment–curvature response is shown in Fig. 20a. Following yielding, the moment is seen to follow a protracted plateau (very similar to stress–strain response) where bending occurs at a mildly increasing moment. At a curvature of $\kappa_L/\kappa_1 = 0.95$, the moment reaches its maximum value. The corresponding Saint-Venant bending strain is 2.03%. Following the maximum, the moment is seen to drop significantly with curvature. The shell buckled at a curvature of $\kappa_c/\kappa_1 = 1.05$.

The ovalizations measured at two points along the shell are shown in Fig. 20b. The two measurements remained essentially the same up to a curvature of approximately $\kappa/\kappa_1 = 0.6$. At higher values of curvature, transducer A, which was later found to be located

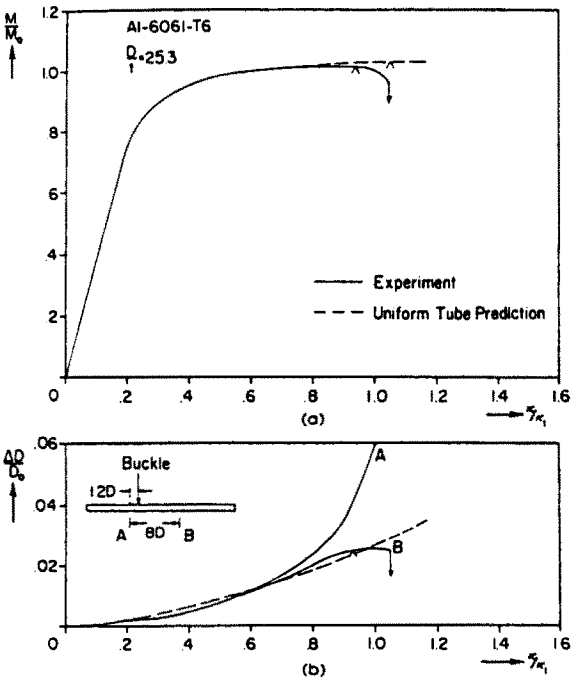

Fig. 20. Bending response of aluminum shell with $D/t = 25.3$: (a) Moment–curvature. (b) Ovalization–curvature.

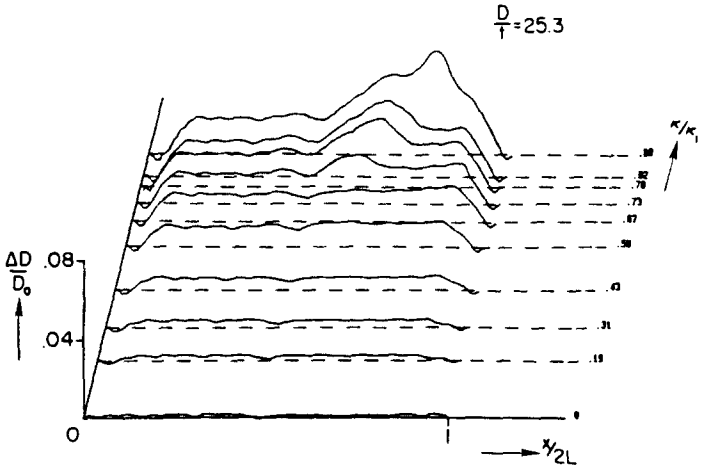

Fig. 21. Ovalization along shell length at different curvatures ($D/t = 25.3$).

close to the position of the final buckle, started to record progressively higher values of ovalization than transducer B. Beyond the limit moment, the ovalizations recorded by the two transducers diverged significantly. At point B, the ovalization eventually started to decrease, indicating local unloading of the shell, whereas at point A, the ovalization started to show signs of unstable growth. The trough of the final buckle was 1.2 diameters from point A. The buckle was characterized by less abrupt gradients than those of the buckles in thinner shells. In addition, the onset of buckling was more gradual and the drop in the post-buckling moment bearing capacity relatively smaller. However, the buckled shell can still be considered to be structurally destroyed. In this case no short wavelength ripples were detected anywhere on the shell. This was also the case for all shells tested with $D/t < 25.3$.

The moment–curvature and ovalization–curvature responses, calculated by the uniform tube analysis, are included in the figures. The predicted limit moment is 12% higher than the measured value, and the ovalization–curvature response is generally in good agreement with the value measured at point B up to the limit moment.

Ovalization scans along the length of a second shell, taken at various values of curvature during the bending history, are shown in Fig. 21. In spite of the obvious presence of some initial geometric imperfections along the shell, the ovalization is seen to remain uniform along the length up to a curvature of approximately $\kappa/\kappa_1 = 0.67$. At $\kappa/\kappa_1 = 0.73$, a section in the middle of the shell, initially approximately five diameters long, started to experience greater ovalization than the rest of the shell. At higher values of curvature, the length of this section grew until, at a curvature of 0.89, it reached a length of approximately 10 diameters. At this curvature, the value of the maximum ovalization was approximately 2.7 times higher than that in the section of shell which remained uniform. The axial position at which the shell localized varied from one specimen to another depending on the position of the most favorable imperfections.

In the case of test specimens which undergo significant localized deformation beyond the limit moment, the global deformation variable, κ, is inappropriate. The rotations of each end of the shell and the axial position of the area of localization can be used to analyze the post limit load response. However, this would complicate the presentation of the results. Thus for convenience, we continue to use κ as the measure of deformation beyond the limit load. The reader is cautioned that this curvature is erroneous to some degree. For the same reason, the curvature at collapse, presented in Table 2, for test specimens 7–11, should only be used for qualitative comparisons.

Results from a shell with D/t of 19.5 are shown in Figs 22 and 23. In this case, the limit moment occurred at $\kappa_L/\kappa_1 = 0.96$, which corresponds to a bending strain of 2.79%. It is interesting to observe that the curvature at the limit moment calculated by the uniform tube analysis is only 5% higher than this value. The ovalization measurements, presented

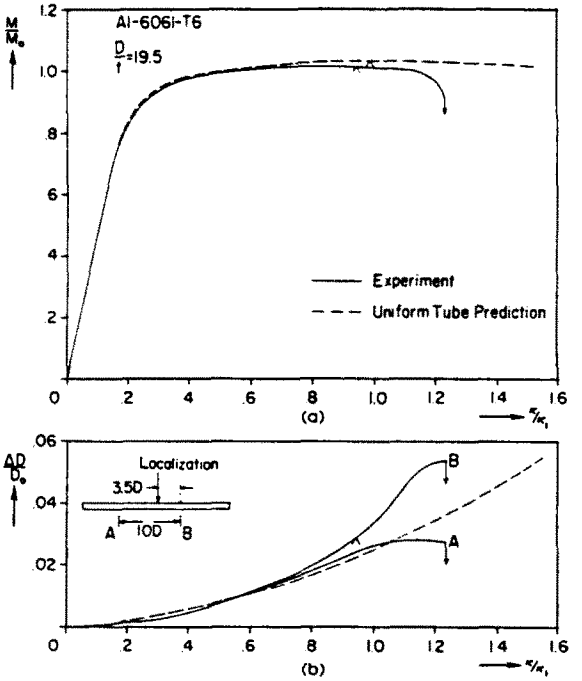

Fig. 22. Bending response of aluminum shell with $D/t = 19.5$: (a) Moment curvature. (b) Ovalization curvature.

in Fig. 22, show the values measured at points A and B to remain very close up to the attainment of the limit moment, beyond which they diverge significantly. As a result of the dropping moment, point A, which was 6.5 diameters away from the trough of localization, experienced a significant decrease in the rate of growth of ovalization and, eventually, the ovalization started decreasing (a point further away from the buckle would experience reduction in ΔD earlier).

Figure 23 shows the axial ovalization scans taken at different values of curvature. The shell is observed to remain uniform up to a curvature of approximately $\kappa/\kappa_1 = 0.75$. At higher curvatures, a section approximately eight diameters long, located in the middle of the shell, starts to ovalize at a faster rate. The rate of growth in this region increases significantly for curvatures higher than $\kappa/\kappa_1 = 0.94$. The length of the localized region, at the last curvature at which a scan was taken, was approximately 10 diameters. After

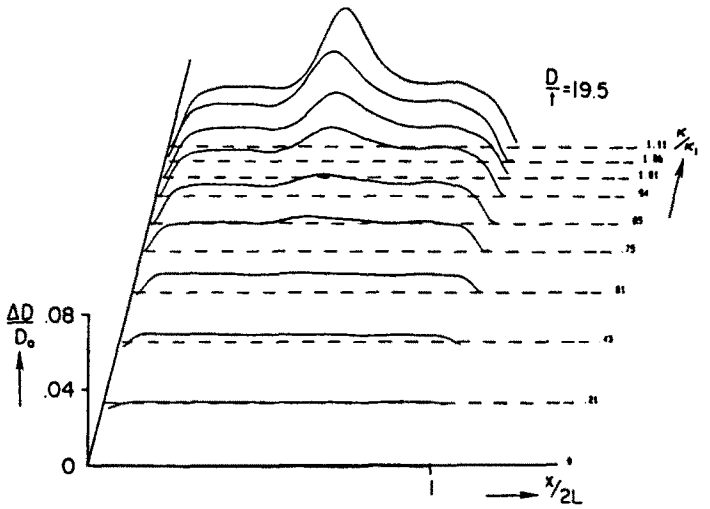

Fig. 23. Ovalization along shell length at different curvatures ($D/t = 19.5$).

significant deformation in the post limit load regime, the shell collapsed. The post-collapse moment bearing capacity was approximately 50% of the limit moment. The collapsed section is shown in Fig. 2b.

DISCUSSION OF THE RESULTS

The experimental results presented demonstrate that the problem is rich in phenomena which are dependent on the D/t of the shell. The problem has an inherent limit load instability which governed the response of some of the shells tested. In addition, short wavelength buckling modes were identified for some shells. In some cases, localization with characteristic lengths of the order of eight to 10 shell diameters was found to interact with short wavelength buckling modes.

In order to highlight the instabilities governing the behavior observed and identify the goals of the analysis, we divide the shells into the following broad categories:

(1) $D/t > 40$†

In this category of relatively thinner shells, the prevalent mode of instability was short wavelength rippling. The curvature (or bending strain) at which the ripples appeared was significantly smaller than that corresponding to the limit load resulting from uniform ovalization. As a result, the two instabilities did not show any signs of interaction. The shells were found to ovalize quite uniformly up to collapse.

The short wavelength ripples appeared in small pockets randomly distributed along the length. They appeared at an increasing moment shortly before the shell collapsed. The amplitude of the ripples grew in a non-uniform fashion (localized). The shells failed catastrophically when a second instability, triggered in one of the ripple pockets, occurred. This happened at a slightly higher value of curvature than κ_b. The collapse mode was characterized by diamond shapes, common in elastic shell buckling. The post-buckling strength of the shells was found to be insignificantly small to be of structural use.

We propose that the observed rippling *qualitatively* corresponds to the axisymmetric buckling mode common in plastic buckling of axially loaded cylindrical shells [see Lee (1962); Batterman (1965); Batterman and Lee (1966)]. For thinner shells, this is followed by a non-axisymmetric buckling mode which leads to catastrophic collapse [see Gellin (1979); Tvergaard (1983)]. The second mode has a characteristic axial wavelength which is twice that of the axisymmetric mode. Qualitatively again, this second buckling mode is similar to the one by which the shells failed catastrophically in the bending experiments.

(2) $26 < D/t < 40$†

In this category of moderately thick shells, the prevalent mode of instability was, again, short wavelength rippling. Unlike the previous category of shells, a well defined limit moment was recorded in the moment–curvature response of these shells. In addition, some non-uniform growth of ovalization was observed just prior to failure for all test specimens in this category. The localized deformation was typically 8–10 diameters long. In a few cases, more than one area of localized deformation was observed to grow simultaneously (probably triggered by initial imperfections). Pockets of short wavelength ripples were usually observed in the trough of the localized region. Following the limit load, the shell buckled catastrophically by the appearance of one sharp, local kink initiated from the ripples.

Two possible explanations can be given for this behavior. The first is based on the observation that the curvature at rippling was progressively closer to the limit load induced by uniform ovalization. Limit loads of this type, which we will call natural, are generally not very imperfection sensitive. However, as will be shown in the second part of this work, some amplification of long wavelength imperfections is possible as the limit load is approached. Thus, conceivably, the growth of long wavelength imperfections observed in the experiments was due to this. The localized ovalization in turn triggered the short

† Approximate values.

wavelength ripples, which made the shell axially more compliant, and caused the limit load to develop earlier.

A somewhat different sequence of events also seems possible at this juncture. It can be argued that the instability which triggers the observed behavior is still rippling. For this range of D/t values, the rippled shells remain stable longer (i.e. the difference between κ_b and κ_c is larger) than thinner ones. The ripples grow, make the shell axially more compliant, and cause a reduction of the overall bending rigidity. This results in the development of the limit load. The presence of the limit load is then responsible for the non-uniform deformation of the shell. Some support for this argument also comes from Calladine (1983). Although he did not address localization of ovalization, he did in essence propose that the ripples cause a reduction in the stiffness of the shell and the development of a limit moment.

These questions will be further addressed in the second part of this study with the help of numerical results.

(3) $D/t < 26$†

The response of this category of relatively thick shells to bending, is governed by the natural limit load instability caused by uniform ovalization. Close to the limit load, long wavelength imperfections tend to be amplified. The ovalization starts to grow non-uniformly along the length and localizes significantly following the limit load. The shell eventually fails in the region of localization. A preliminary conclusion is that the localization is a direct consequence of the limit load instability and affects the behavior of the shell primarily after the limit load. Thus, the limit load calculated by assuming the shell to ovalize uniformly is very representative of the actual value.

The bounding D/t values of the three categories of shell behavior are only approximate and, very definitely, vary with the shell material properties.

DESIGN CONSIDERATIONS

The discussion above clearly demonstrates the complexity of plastic buckling and various mechanisms of collapse of shell structures. Simulation and prediction of the instabilities discussed is of great fundamental interest, and if successfully carried out should improve the general understanding of the problem area. However, the predictions will obviously be complicated by the three-dimensional nature of the mechanical phenomena involved.

It is possible that a simpler approach may adequately serve the needs of structural design. The two main instabilities observed experimentally are the short wavelength rippling and the limit moment resulting from uniform ovalization. Thus, as a first step, the uniform tube analysis of Shaw and Kyriakides (1985) was used to calculate the limit moment, the corresponding curvature and Saint-Venant bending strain for shells with D/ts ranging from 15 to 100. The average values of the key material parameters of the shells tested, and listed below, were used in these calculations:

$$E = 10^4 \text{ ksi (68.95 GPa)}, \quad \sigma_y = 42.6 \text{ ksi (293.7 MPa)}, \quad n = 29 \quad \text{and} \quad \nu = 0.32.$$

Following Reddy (1979), the calculated maximum Saint-Venant bending strain corresponding to the limit moment is plotted against D/t (log-log scales) in Fig. 24. The critical strains measured in the 11 experiments (i.e. either ε_L or ε_b) are also included in the same figure. (Note that due to the ovalization of the cross-section the actual critical axial bending strain in the shells is 2–3% lower than the maximum Saint-Venant bending strain.)

An independent bifurcation check analysis developed by Ju and Kyriakides (1991) was incorporated in the uniform tube bending analysis mentioned above. This was used to identify the onset of ripple-like bifurcations during the bending history. The buckling mode used is as follows:

† Approximate value.

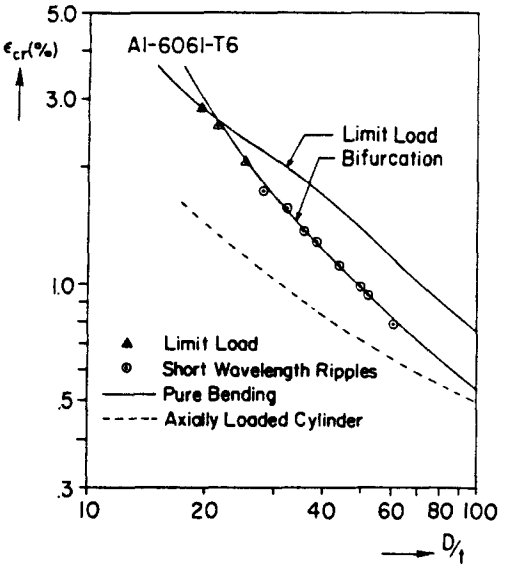

Fig. 24. Critical maximum Saint-Venant bending strain as a function of shell D/t. Comparison of experimental values and various predictions.

$$\tilde{w} = R\cos px \sum_{n=0}^{N_w} c_n \cos n\theta,$$

$$\tilde{v} = R\cos px \sum_{n=1}^{N_v} d_n \sin n\theta, \quad p = \frac{\pi}{\lambda_D},$$

$$\tilde{u} = R\sin px \sum_{n=0}^{N_u} e_n \cos n\theta, \tag{5}$$

where $\{\tilde{u}, \tilde{v}, \tilde{w}\}$ are displacements in the axial, circumferential and radial directions, measured from a circular toroidal reference shell with the following principal curvatures:

$$\kappa_1 = \frac{\kappa\cos\theta}{1+\kappa R\cos\theta} \quad \text{and} \quad \kappa_2 = \frac{1}{R}. \tag{6}$$

κ, in eqn (6) is the curvature of the bent tube at the time of the bifurcation test. The formulation used is based on Sanders' (1963) non-linear shell kinematics. As is customary, the J_2 deformation theory of plasticity, with the state of stress calculated in the tube analysis, was used in the bifurcation check together with Hill's concept of comparison solid [see Hill (1958)].

The critical bifurcation strains, calculated for the same group of shells mentioned above, are included in Fig. 24. For this material, the calculated bifurcation strain is lower than the strain corresponding to the limit load for shells with $D/t > 22$. For shells with lower D/t values, the calculated limit load precedes the bifurcation instability. The correlation of the predictions with the experimental results is exceptionally good. A small difference in the value of the transitional D/t exists, in that no ripples were observed in the experiments for shells with $D/t < 25.7$. This difference is partly due to variations in material properties from shell to shell. As in other plastic bifurcation problems [see Hutchinson (1974)], the corresponding bifurcation strains calculated by using the J_2 flow theory are unreasonably high for thinner shells and do not exist for thicker shells in the range of D/ts studied.

The same degree of agreement between experimental and predicted critical strains has been obtained for steel shells. However, the transitional D/t was, in general, higher than in the aluminum shells. Similar success of this simplified approach was also demonstrated for the problem of bending under external pressure in Corona and Kyriakides (1988) and Ju and Kyriakides (1991). It can thus be concluded that, in spite of the simplicity of the

approaches followed, the limit load and ripple bifurcation predictions constitute very useful tools for establishing the limit to which long shells can be safely bent.

Another simplification, often made in the literature, is to use the critical strain at which axially-loaded circular cylindrical shells first buckle into an axisymmetric mode as the critical design strain of shells in bending [e.g. Seide and Weingarden (1961) for elastic shells; Reddy (1979), Yun and Kyriakides (1990) for elastic–plastic shells]. The critical axial stress of this problem is given by

$$\sigma_c = \left[\frac{C_{11}C_{22} - C_{12}^2}{3}\right]^{1/2}\left(\frac{2t}{D}\right). \tag{7}$$

The corresponding critical axial half wavelength is given by

$$\lambda_c = \pi\left[\frac{C_{11}^2}{12(C_{11}C_{22} - C_{12}^2)}\right]^{1/4}\left(\frac{Dt}{2}\right)^{1/2} \tag{8}$$

where $C_{\alpha\beta}$ are the instantaneous moduli of the material at bifurcation (in our case, calculated by J_2 deformation theory). The critical strain can be evaluated from (7) and (3).

The critical strains predicted, using this approach, are also shown in Fig. 24. As might be expected, in the range of D/t values considered, these predictions represent a lower bound to the experimental results. For lower D/ts the predictions are low by a factor of two. At higher D/t values, they approach the bifurcation predictions obtained from the tube analysis mentioned above. In view of this, for aluminum 6061-T6 shells with $D/t < 80$ (approximately) the analysis which includes the effect of ovalization should be preferred over eqns (7) and (8).

In a number of recent publications, investigators have explored design schemes for assessing the post-buckling strength of tubular structures. We stress that pure bending experiments on both steel and aluminum tubes have clearly shown that, following local buckling, the moment and deformation capacity of shells is structurally insignificant. Persistent rotation of the ends of the shell results in a continued drop in moment and eventually leads to fracture and total failure. This is due to the very localized nature of the deformations imposed on the shell by buckling. Although the post-buckling strength of tubular components which are more constrained by the remainder of the structure should be somewhat better, the essence of the statements above is unaltered. Thus the post-buckling regime should be tackled with great caution.

Acknowledgement—The work presented was conducted with financial support from the U.S. Office of Naval Research under contract N00014-88-K-0610.

REFERENCES

Ades, C. S. (1957). Bending strength of tubing in the plastic range. *J. Aero. Sci.* **24**, 605–620.
Axelrad, E. L. (1980). Flexible shells. *Proc. 15th IUTAM Congress*, Toronto, Canada, pp. 45–56.
Batterman, S. C. (1965). Plastic buckling of axially compressed cylindrical shells. *AIAA Jl* **3**, 316–325.
Batterman, S. C. and Lee, L. H. N. (1966). Effects of modes on plastic buckling of compressed cylindrical shells. *AIAA Jl* **4**, 2255–2257.
Brazier, L. G. (1927). On the flexure of thin cylindrical shells and other thin sections. *Proc. Roy. Soc.*, Series A, **116**, 104–114.
Bushnell, D. (1981). Elastic-plastic bending and buckling of pipes and elbows. *Comp. Struct.* **13**, 241–248.
Calladine, C. R. (1983). Plastic buckling of tubes in pure bending. In *Proceedings of the IUTAM Conference on Collapse* (Edited by G. W. Hunt and J. M. T. Thompson), pp. 111–124. Cambridge University Press, London, U.K.
Corona, E. and Kyriakides, S. (1988). On the collapse of inelastic tubes under combined bending and pressure. *Int. J. Solids Structures* **24**, 505–535.
Fabian, O. (1977). Collapse of cylindrical, elastic tubes under combined bending, pressure and axial loads. *Int. J. Solids Structures* **13**, 1257–1270.
Fabian, O. (1981). Elastic-plastic collapse of long tubes under combined bending and pressure load. *Ocean Engng* **8**, 295–330.
Gellin, S. (1979). Effect of an axisymmetric imperfection on the plastic buckling of an axially compressed cylindrical shell. *ASME J. Appl. Mech.* **46**, 125–131.

Gellin, S. (1980). The plastic buckling of long cylindrical shells under pure bending. *Int. J. Solids Structures* **10**, 397–407.

Hill, R. (1958). A general theory of uniqueness and stability of elastic-plastic solids. *J. Mech. Phys. Solids* **6**, 236–249.

Hutchinson, J. W. (1974). Plastic buckling. *Adv. Appl. Mech.* **14**, 67–144.

Jirsa, J. O., Lee, F. K., Wilhoit, J. C. and Merwin, J. E. (1972). Ovaling of pipelines under pure bending. OTC 1569, *Proc. Offshore Tech. Conf.* **I**, 573–578.

Johns, T. G., Mesloh, R. E., Winegardener, R. and Sorenson, J. E. (1975). Inelastic buckling of pipelines under combined loads. OTC 2209, *Proc. Offshore Tech. Conf.* **II**, 635–646.

Ju, G. T. and Kyriakides, S. (1991). Bifurcation buckling vs limit load instabilities of elastic-plastic tubes under bending and external pressure. *ASME J. Offshore Mech. Arctic Engng* **113**, 43–52.

Kyriakides, S. and Shaw, P. K. (1987). Inelastic buckling of tubes under cyclic bending. *ASME J. Pressure Vessel Tech.* **109**, 169–178.

Kyriakides, S. and Yeh, M. K. (1988). Plastic anisotropy in drawn tubes. *ASME J. Engng Industry* **110**, 303–307.

Lee, L. H. N. (1962). Inelastic buckling of initially imperfect cylindrical shells subject to axial compression. *J. Aero. Sci.* **29**, 87–95.

Moore, R. L. and Clark, J. W. (1952). Torsion, compression, and bending tests of tubular sections machined from 75S-T6 rolled round rod. NACA RM 52I25.

Reddy, B. D. (1979). An experimental study of the plastic buckling of circular cylinders in pure bending. *Int. J. Solids Structures* **15**, 669–685.

Sanders, J. L. (1963). Nonlinear theories of thin shells. *Q. Appl. Math.* **21**, 21–36.

Seide, P. and Weingarden, V. I. (1961). On the buckling of circular cylindrical shells under pure bending. *ASME J. Appl. Mech.* **28**, 112–116.

Shaw, P. K. and Kyriakides, S. (1985). Inelastic analysis of thin-walled tubes under cyclic bending. *Int. J. Solids Structures* **21**, 1073–1100.

Sherman, D. R. (1976). Tests of circular steel tubes in bending. *ASCE J. Struct. Div.* **102**, ST11, 2181–2195.

Stephens, W. B., Starnes, J. H. and Almorth, B. O. (1975). Collapse of long cylindrical shells under combined bending and pressure loads. *AIAA Jl* **13**, 20–25.

Tuggu, P. and Schroeder, J. (1979). Plastic deformation and stability of pipes exposed to external couples. *Int. J. Solids Structures* **15**, 643–658.

Tvergaard, V. (1983). Plastic buckling of axially compressed circular cylindrical shells. *Thin-Walled Struct.* **1**, 139–163.

Yun, H. and Kyriakides, S. (1990). On the beam and shell modes of buckling of buried pipelines. *Int. J. Soil Dynamics Earthquake Engng* **9**, 179–193.